Suzaku Discovery of Hard X-ray Pulsations from the Rotating Magnetized White Dwarf, AE Aquarii

Yukikatsu Terada,[1] Takayuki Hayashi,[2] Manabu Ishida,[3] Koji Mukai,[4]
Tadayasu Dotani,[3] Shunsaku Okada,[3] Ryoko Nakamura,[3]
Sachindra Naik,[5] Aya Bamba,[3] and Kazuo Makishima[6,7]

[1] *Department of Physics, Science, Saitama University, Saitama 338-8570*
[2] *Science of Physics, Tokyo Metropolitan University,*
1-1 Minami-Osawa, Hachioji-si, Tokyo, 192-0397, Japan
[3] *Department of High Energy Astrophysics,*
Institute of Space and Astronautical Science (ISAS),
Japan Aerospace Exploration Agency (JAXA),
3-1-1 Yoshinodai, Sagamihara, Kanagawa 229-8510, Japan
[4] *Exploration of the Universe Division, Code 660,*
NASA/GSFC, Greenbelt, MD 20771, USA
[5] *Physical Research Laboratory, Ahmedabad 380 009, India*
[6] *Makishima Cosmic Radiation Laboratory, RIKEN,*
2-1, Hirosawa, Wako-shi, Saitama 351-0198, Japan
[7] *Department of Physics, Graduate School of Science,*
University of Tokyo, Hongo 7-3-1, Bunkyo-ku, Tokyo 113-0033, Japan
terada@phy.saitama-u.ac.jp

Abstract

The fast rotating magnetized white dwarf, AE Aquarii, was observed with Suzaku, in October 2005 and October 2006 with exposures of 53.1 and 42.4 ks, respectively. In addition to clear spin modulation in the 0.5–10 keV band of the XIS data at the barycentric period of 33.0769 ± 0.0001 s, the 10–30 keV HXD data in the second half of the 2005 observation also showed statistically significant periodic signals at a consistent period. On that occasion, the spin-folded HXD light curve exhibited two sharp spikes separated by ~ 0.2 cycles in phase, in contrast to approximately sinusoidal profiles observed in energies below ~ 4 keV. The folded 4–10 keV XIS light curves are understood as a superposition of those two types of pulse profiles. The phase averaged 1.5–10 keV spectra can be reproduced by two thermal components with temperatures of $2.90^{+0.20}_{-0.16}$ keV and $0.53^{+0.14}_{-0.13}$ keV, but the 12-25 keV HXD data show a significant excess above the extrapolated model. This excess can be explained by either a power-law model with photon index of $1.12^{+0.63}_{-0.62}$ or a third thermal component with a temperature of 54^{+26}_{-47} keV. At a distance of 102 pc, the 4–30 keV luminosities of the thermal and the additional components become $1.7^{+1.3}_{-0.6}$ and $5.3^{+15.3}_{-0.3} \times 10^{29}$ erg s^{-1}, respectively. The latter corresponds to 0.09% of the spin down energy of the object. Possible emission mechanisms of the hard pulsations are discussed, including in particular non-thermal ones.

Key words: acceleration of particles – stars: white dwarfs – X-rays: individual (AE Aquarii)

1. Introduction

Since the discovery of cosmic-rays by Hess in 1912, the origin of such high-energy particles and the mechanism of their acceleration have remained a long-standing issue in astrophysics. Among various types of astrophysical particle acceleration sites, one important prototype is rotation-powered pulsars, namely fast rotating neutron stars (NSs) with strong magnetic field of $\geq 10^{12}$ G. They are considered to accelerate particles using their rotation as the ultimate energy source, and strong electric fields as the acceleration tool. The electrostatic potential, induced by the strong surface field, B, and the fast rotation with a period, P, is expected to amount to

$$V \sim \left(\frac{2\pi R}{P} \right) BR$$

$$\sim 6 \times 10^{16} \left(\frac{P}{1\text{s}} \right)^{-1} \left(\frac{B}{10^{12}\text{G}} \right) \left(\frac{R}{10^{6}\text{cm}} \right)^{2} \text{V} \qquad (1)$$

where R is a typical radius from the NS center at which the electric acceleration takes place.

Magnetized white dwarfs (WDs) are similar systems to pulsars; rotating compact objects with strong magnetic fields. Since a typical magnetized WD has $P \sim 5 \times 10^{3}$ s, $B \sim 10^{6}$ G, and $R \geq 10^{9}$ cm, we expect $V \sim 10^{13}$ V from equation (1). Therefore, magnetized WDs should be a promising candidate of new particle acceleration sites, although efficiencies of the particle acceleration and the

subsequent radiation could be different between pulsars and WDs.

Non-thermal incoherent radio emission has in fact been detected from seven WDs via systematic radio surveys (Nelson and Spencer 1988; Beasley et al. 1994; Pavelin et al. 1994; Bond et al. 2002; Mason and Gray 2007). Some objects like AE Aquarii (Bastian et al. 1988; Abada-Simon et al. 1993) and AM Herculis (Chanmugam and Dulk 1982; Dulk et al. 1983) show signs of coherent radio emission. Then, higher-energy photons in the X-ray to gamma-ray bands may also be generated via such non-thermal processes as curvature radiation like in NSs, non-thermal bremsstrahlung, and inverse Compton scattering of soft photons (Chanmugam and Brecher 1985; Cheng and Ruderman 1991; Ikhsanov and Biermann 2006), as well as electron-positron annihilation lines and γ-ray emission via the π^0 decay chain. In fact, some authors reported TeV gamma-ray emission from AE Aquarii and AM Herculis during optical flares (Meintjes et al. 1992; Meintjes et al. 1994; Bhat et al. 1991). Therefore, high energy electrons with energies reaching 1-100 MeV are thought to be present in these WDs (Abada-Simon et al. 1993; Meintjes and Venter 2003).

The object AE Aquarii (hereafter AE Aqr), located at a distance of $d = 102^{+42}_{-23}$ pc (Friedjung 1997), is a magnetized cataclysmic variable (MCV) belonging to the DQ Herculis (or intermediate polar) class. It is spinning near break up (de Jager 1994) with a spin period of $P_{\rm sp} = 33.0767$ s (Patterson 1979), which is the second fastest value among MCVs. This fast rotation, combined with the surface field intensity of $B \sim 10^{5-6}$ G which is a typical value among intermediate polars, yields via equation (1) an induced potential of $V \simeq 10^{14-15}$ V, which is probably one of the highest found among MCVs. In addition, AE Aqr has been in a spin-down state over the past 27 years, at a rather high rate of 1.8×10^{-6} s yr^{-1} (de Jager et al. 1994; Mauche 2006). The value implies a huge spin-down luminosity of 6×10^{33} erg s^{-1} (de Jager 1994; de Jager et al. 1994). The object is one of the most asynchronous cataclysmic variables with an orbital period of $P_{\rm orb} = 35567$ s $= 9.88$ hr (Casares et al. 1996; de Jager et al. 1994). Flares reported in the radio band (Bastian et al. 1988; Abada-Simon et al. 1993) are consistent with synchrotron emission (Meintjes and Venter 2003), and the pulsating TeV gamma-rays (Meintjes et al. 1992; Meintjes et al. 1994) are sometimes coincident with optical flares.

According to soft X-ray observations (Ezuka and Ishida 1999; Itoh et al. 2006), the plasma temperature of thin thermal radiation from AE Aqr is significantly lower than the estimated gravitational potential of its WD, whose mass is about 0.8 – 0.9 times the solar mass (Casares et al. 1996; Welsh et al. 1995). Furthermore, its UV to X-ray luminosity (10^{31} erg s^{-1}) is three orders of magnitude lower than that in a simple accretion case (Eracleous and Horne 1996) with a rate of 10^{17} g s^{-1}. Therefore, the accreting matter may be inhibited from reaching the WD surface by the fast WD rotation (Itoh et al. 2006). Wynn et al. (1997) argue that only 1 % of the accreting gas in AE Aqr reaches the WD surface, while the rest is expelled

away due to propeller effects. These observed properties altogether suggest strongly that AE Aqr is a promising site of particle acceleration, as pointed out by de Jager (1994).

The hard X-ray band is most suited to the search for the expected non-thermal signals, because that particular band is expected to receive the largest number of non-thermal high-energy photons without being hampered by the soft X-rays arising from accretion. In the present paper, we report on the first successful detection of pulsating hard X-rays from the most promising object, AE Aqr, achieved with Suzaku (Mitsuda et al. 2007), which carries two instruments; the X-ray CCD camera called the X-ray Imaging Spectrometer (XIS;Koyama et al. 2007) with the X-ray telescope (XRT; Serlemitsos et al. 2007) and the Hard X-ray Detector (HXD;Takahashi et al. 2007). The emission is likely to be of non-thermal origin, thus reinforcing the view that MCVs are indeed particle accelerators.

2. Observation and Data Reduction

2.1. Suzaku Observation of AE Aqr

We observed AE Aqr with Suzaku twice during the performance verification phase. The first observation was performed from 2005 October 30 02:13 UT to November 2 01:02 UT (sequence number 400001010), and the second one from 2006 October 25 5:25 UT to 09:11 UT on the next day (sequence number 400001020). The observations were carried out at the "HXD nominal" pointing position (i.e., with the target on the nominal optical axis of the HXD). Although the HXD has no imaging capability, the full field of view of its PIN diodes (1.0 degrees square) contained no hard X-ray objects in the Swift BAT catalog. On both occasions, the XIS was operated in the normal mode with the "1/8 window" option, which gives a time resolution of 1 s, without charge injection function. The HXD was operated in the nominal mode; in the second observation, however, a quarter of the 64 PIN diodes were operated with a reduced voltage of 400 V, rather than the nominal 500 V.

2.2. Data Reduction

We used the datasets produced by the Suzaku pipeline processing version 1.2.2.3 with the calibration-version of hxd20060829, xis20060913, xrt20060720, and xrs20060410, using tools in HEADAS package version 6.2. We used XSPEC version 11.3.2, to fit spectra with models.

The source was detected with the XIS in the 0.5 – 10 keV band at an intensity of 0.37 c s^{-1} and 0.28 c s^{-1} per sensor, in 2005 and 2006, respectively. In the XIS analysis, we excluded all telemetry-saturated data portions, and data taken in "low" data-rate mode. We further removed those intervals when the source elevation above Earth's limb was below 5°, Earth's day-night boundary was less than 25°, or the spacecraft was in, and 436 s after, leaving the South Atlantic Anomaly (SAA). We then accumulated nominal-grade events within 6 mm (4ʹ3) of the image centroid. The XIS background events were taken

from a source-free region of the corresponding sensor. The derived background, exhibiting a rate of ~ 0.02 c s^{-1} per sensor in 0.5–10 keV, is generally negligible except in the highest end of the XIS bandpass.

In calculating XIS ancillary response files, we took into account efficiency reduction caused by the window option and by un-controlled fluctuations of the optical axis of the XRT (Serlemitsos et al. 2007). In the first observation, the effective areas of XIS-0, 1, 2, and 3 were thus reduced to 92.3%, 93.1%, 93.4%, and 93.7% of their nominal values, respectively, while those during the second observation were 93.7%, 93.2%, 92.8%, and 93.8% respectively.

The HXD data were screened using the same criteria as used on the XIS data. In addition, we discarded data acquired during time intervals when the geomagnetic cutoff rigidity was lower than 8 GV. After these filtering steps, the final event list of HXD-PIN was obtained using only those events that survived the standard anti-coincidence function of the HXD (DET_TYPE=1). The non X-ray background (NXB) of HXD-PIN was synthesized by appropriately combining night-Earth data sets acquired under different conditions (Kokubun et al. 2007), using METHOD='PINUDLC' and version of METHODV=1.2 (Watanabe et al. 2007).

After selecting event lists, the first observation yielded net exposures of about 70.3 and 53.1 ks with the XIS and the HXD, respectively. Those in the second observation were 48.6 with the XIS, and 42.4 ks with the HXD.

3. Timing Analyses

3.1. Light Curves

Background-subtracted light curves of AE Aqr, obtained with the XIS and the HXD, are shown in figure 1. From this figure, it is not obvious whether the source is detected with HXD-PIN. More quantitatively, the background-subtracted 13–30 keV PIN counts integrated over 1 ks become $14.0 \pm 14.5 \pm 4.0$ c ks^{-1} and $18.0 \pm 20.9 \pm 6.0$ c ks^{-1}, in 2005 and 2006, respectively; where the first uncertainties are statistical 90% errors, while the second ones are systematic errors in the PIN NXB subtraction estimated from the reproducibility of counts during the satellite pointing at Earth. For reference, the PIN NXB counts in the same energy range were 198 and 202 c ks^{-1} in 2005 and 2006, respectively. Therefore, the source detection with HXD-PIN becomes significant both in the 2005 and 2006 observations when integrated over the full exposure of ~ 50 ks. However, the detection becomes marginal when we consider contribution from the cosmic X-ray background (CXB) which is estimated to be 18.0 c ks^{-1} in the 13–30 keV PIN band, based on its canonical surface brightness (Boldt 1987) and the angular response of the PIN diodes to uniform illumination. Aiming at a higher detection sensitivity, below we search the data for periodic modulations synchronized with the WD rotation, before carrying out spectral analyses.

In both observations, the XIS data reveal several flares involving two- to three-fold intensity increases, each last-

ing for ~ 2500 s. In the PIN data, however, no corresponding flux increases are found, primarily because of insufficient count statistics. Even if PIN counts increased by a factor of 3 in 2500 s (maximum ~ 38 c per 25 ks), the associated statistical errors, ~ 36 c, would be comparable.
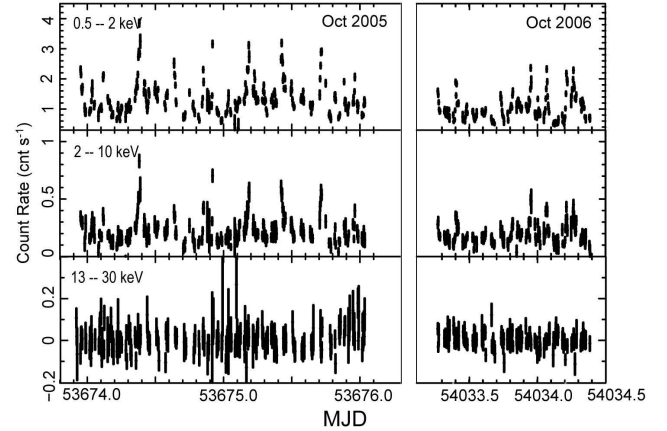

Fig. 1. Background-subtracted light curves of AE Aqr during the two observations, obtained with the XIS (0.5 − 2 keV and 2 − 10 keV) and the HXD (13 − 30 keV). The HXD data are corrected for dead time. The XIS and HXD-PIN data are binned into 250 s.

3.2. XIS Period Determination

After applying the standard barycentric corrections to the photon arrival times (Terada et al. 2008), we searched the XIS light curves extracted from the source region for periodic intensity variations synchronized with the WD rotation. In doing so, we did not subtract the background, because the background events occupy only 5.0% of the total count rate of the XIS, and no periodicity around $P_{\rm sp}$ was found in the background data. The standard epoch-folding analysis of the 0.5–10 keV XIS data revealed highly significant source pulsations on both occasions, at a barycentric period of $P_{\rm XIS} = 33.0769$ s. After Larsson (1996), 68% errors associated with these period determinations are estimated to be 0.0063 s and 0.0104 s, in 2005 and 2006, respectively. Within these errors, the derived period is consistent with the values of $P_{\rm sp}$ measured in the optical (Patterson 1979; de Jager et al. 1994), in X-rays with Ginga, ASCA (Choi et al. 1999), XMM-Newton (Itoh et al. 2006), and Chandra (Mauche 2006), and in TeV γ-rays (Meintjes et al. 1992). Therefore, we identify $P_{\rm XIS}$ with the rotational period of the WD in AE Aqr; that is, $P_{\rm XIS} = P_{\rm sp}$.

Figure 2 (top) shows 0.5–10 keV XIS periodograms, used in determining $P_{\rm XIS}$. Strictly speaking, the above period determinations utilized the full length of the 2005 and 2006 data sets, while the periodograms in this figure were obtained with the 2005 data divided into the first and second halves (hereafter 2005a and 2005b, respectively), each having a 90.2 ks gross duration, and a net exposure of 26.4 and 34.6 ks, respectively. The very similar shapes of the three (2005a, 2005b, and 2006) XIS periodograms indicate that the periodic modulation in the
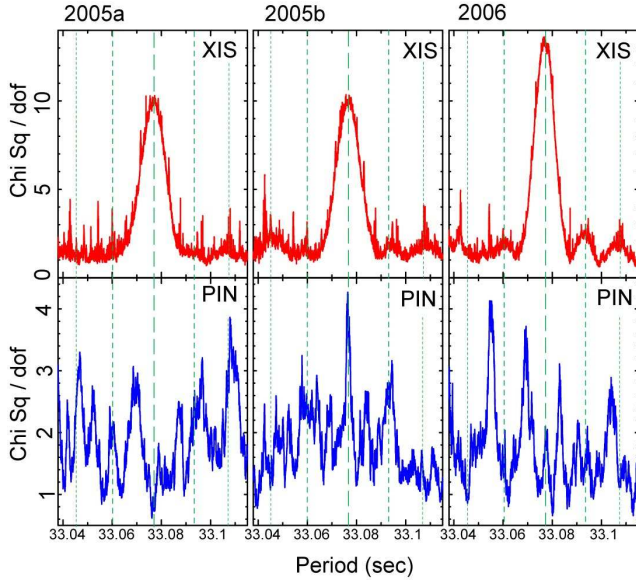
Fig. 2. Periodograms calculated from the background-inclusive XIS data (red) and the HXD-PIN data (blue). The vertical axis shows reduced χ^2, calculated against a hypothesis that the folded data profile is constant. The period step is 2.5×10^{-5} s, using 7 and 64 bins per cycle for the XIS and HXD, respectively. The vertical green lines indicate various expected periods; the spin period P_{SP} (thick dashed); P_{pro} and P_{ret} (thin dashed); and the beat periods between P_{SP} and 1 day (dotted). (left) Results from the first half of the 2005 data, where the PIN energy band is $10 - 30$ keV. (middle) The same as left panel, but for the second half of the 2005 observation. (right) Results from the entire 2006 observation, where the PIN energy band refers to $13 - 30$ keV.

XIS band is quite stable. Although we could in principle determine the period with a much higher accuracy by coherently combining the 2005 and 2006 datasets, the periods on individual occasions are too uncertain to extrapolate them for one year without pulse-count ambiguities. Instead, we incoherently combined the 2005 and 2006 periodograms, which reduced the period error to 0.0001s (Larsson 1996). We hence quote the XIS-determined period as $P_{XIS} = 33.0769 \pm 0.0001$ s.

In energies below 2 keV, the pulse-peak phase comes at BJD (Barycentric Julian Ephemeris Day) $2453673.5000134 \pm 0.0000011$, from the combined dataset of 2005 and 2006 folded on the period of P_{XIS}. When this epoch and the above determined P_{XIS} are employed, our measurement predicts the pulse peak to occur at BJD 2453613.2767025 during the Chandra observation conducted on 2005 August 31. This agrees, within 0.0000033 days, or 0.29 s with that actually measured on that occasion by Mauche (2006), namely BDJ $2453613.2767058 \pm 0.0000039$.

The XIS light curves, folded on the spin period P_{XIS}, are presented in figure 3 in several energy bands. Thus, the modulation at lower energies has a sinusoidal profile, with an amplitude of $\sim \pm 16\%$ of the mean intensity. Toward higher energies, the folded pulse profiles become more structured; this may be responsible for the fine structures seen in the XIS periodograms (figure 2). Further analysis

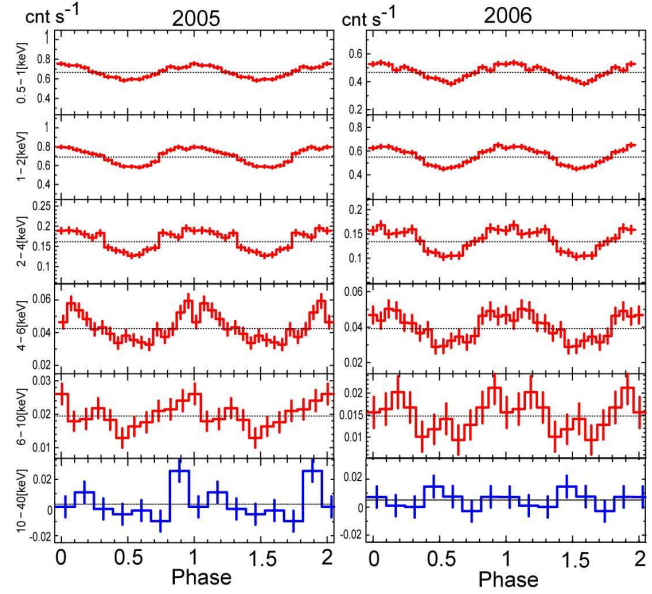of the folded pulse profiles is conducted in subsection 3.4.

Fig. 3. Energy-resolved light curves folded on the XIS-determined period of 33.0769 s. The non X-ray backgrounds are subtracted from the XIS data, but not from the HXD-PIN data. The energies from top to bottom panels are $0.5 - 1$ keV, $1 - 2$ keV, $2 - 4$ keV, $4 - 6$ keV, and $6 - 10$ keV for the XIS, while $10 - 40$ keV or $13 - 40$ keV with the HXD for the 2005 and 2006 observations, respectively. The vertical axis shows the count rate in each energy band, with the maximum scale set to 1.3 times the averaged count rate of that band. Phase 0.0 corresponds to BJD 2453673.5000, and the date of the pulse peak in the 0.5-2 keV band (at a spin phase of 0.035) occurs on BJD 2453673.5000134 $\pm$ 0.0000011.

3.3. HXD Period Search

After the same barycentric corrections, we folded background-inclusive PIN data on the period of P_{XIS}. The 2005 data were analyzed in an energy range of 10–30 keV, while those of 2006 in 13–30 keV, because thermal noise arose around the PIN lower threshold level in this observation. Since the PIN data have much poorer signal statistics, we tentatively divided the period into seven phase bins. Then, as shown in figure 3 (bottom) in blue, a statistically significant modulation with a spiky profile was found from the 2005 data with a reduced chi-squared of $\chi_\nu^2 = 2.5$ for $\nu = 6$, whereas the 2006 data was consistent with being constant ($\chi_\nu^2 = 0.62$).

Now that the PIN signals exhibit a hint of periodic modulation at the period of P_{XIS} at least in the first observation, we proceed to more systematic epoch-folding analyses on the background-inclusive 10–30 keV (or 13–30 keV) PIN light curves. The reason for not subtracting the background is that the actual background would not vary significantly in 30 s (Kokubun et al. 2007), and that the synthetic PIN background models have larger uncertainties when used on time scales of ~ 1 s, as would be needed here. Specifically, we calculated HXD periodograms over a trial period range of 33.04 to 33.12 s,

with a typical period step of 2.5×10^{-5} s or even finer. The bin number per cycle was varied in the range between 7 and 13. Furthermore, to avoid false quantization effects due to finite phase bin numbers, we calculated, at each trial period, chi-squares by changing the time origin within a single phase bin, and then selected the maximum value to construct the periodogram. Typical results from these studies are shown in figure 2 in blue, in comparison with those from the XIS data. Thus, the three (2005a, 2005b, and 2006) PIN periodograms all exhibit multiple peaks reaching $\chi_\nu^2 = 3 - 4$. Therefore, the PIN signals are inferred to be significantly variable on times scales of ~ 33 s, possibly involving rather rapid variations as suggested by the narrow widths of these peaks.

The most important finding from these studies is that the 2005b PIN periodogram exhibits its highest peak with $\chi_\nu^2 = 4.2$ (for $\nu = 6$) at a period of $P_{\rm HXD} = 33.0764 \pm 0.0005$ s, which agrees well with $P_{\rm sp}$, and hence $P_{\rm XIS}$ within respective errors. The probability of this peak arising by chance is lower than 7×10^{-7}. Although the results presented here were obtained using a particular 7 phase bins per cycle, the results do not change if different numbers of bins (e.g., 8, 11, or 13) are utilized. The reason why the PIN profile in figure 3 exhibited $\chi_\nu^2 = 2.5$ instead of the peak value ($\chi_\nu^2 = 4.2$) is that it was calculated at $P_{\rm XIS}$ rather than $P_{\rm HXD}$. The peak at $P_{\rm HXD}$ does not disappear even if we divide the 2005b data into two halves each comprising 32 PIN detectors. Furthermore, side lobes seen at 33.060 s and 33.092 s in the 2005b plot can be interpreted as due to beat between $P_{\rm sp}$ and the Suzaku sampling window. These facts suggest that the periodic signal at $P_{\rm HXD}$ in the 2005b PIN data is real, and is intrinsic to the WD rotation. The narrower peak in the PIN periodogram compared to that of the XIS, is consistent with the folded PIN profile having sharp structures, as already suggested by figure 3. In contrast, the PIN signal modulation at $P_{\rm sp}$ is not significant either in the 2005a or the 2006 data.

3.4. Pulse Profiles

We have so far obtained promising evidence that the PIN signals are indeed modulated at $P_{\rm sp}$. Of course, the peak in the 2005b periodogram (figure 2) could be an accidental coincidence caused by some non-periodic hard X-ray variations, considering the presence of multiple peaks in the other PIN periodograms. However, in figure 3, the XIS profiles become similarly structured toward higher energies. Therefore, we expect that the hard X-ray periodicity can be reinforced by comparing the folded PIN profiles with those from the XIS in harder energies.

We sorted the XIS data into two bands (0.5–4 keV and 4–10 keV), and folded them both at the period of $P_{\rm HXD}$. For reference, we also folded the 2005 HXD-PIN data in 10–30 keV at the same period, with the same bin size as for the XIS data, namely 29 bins per cycle. The folded profiles derived in the three energy bands are presented in figure 4. As already suggested by figure 3, the PIN profiles indeed exhibit several sharp spikes, among which at least two, one at a pulse phase of $\phi \sim 0.9$ and the other at $\phi \sim 0.1$, are statistically significant. As shown in figure 4
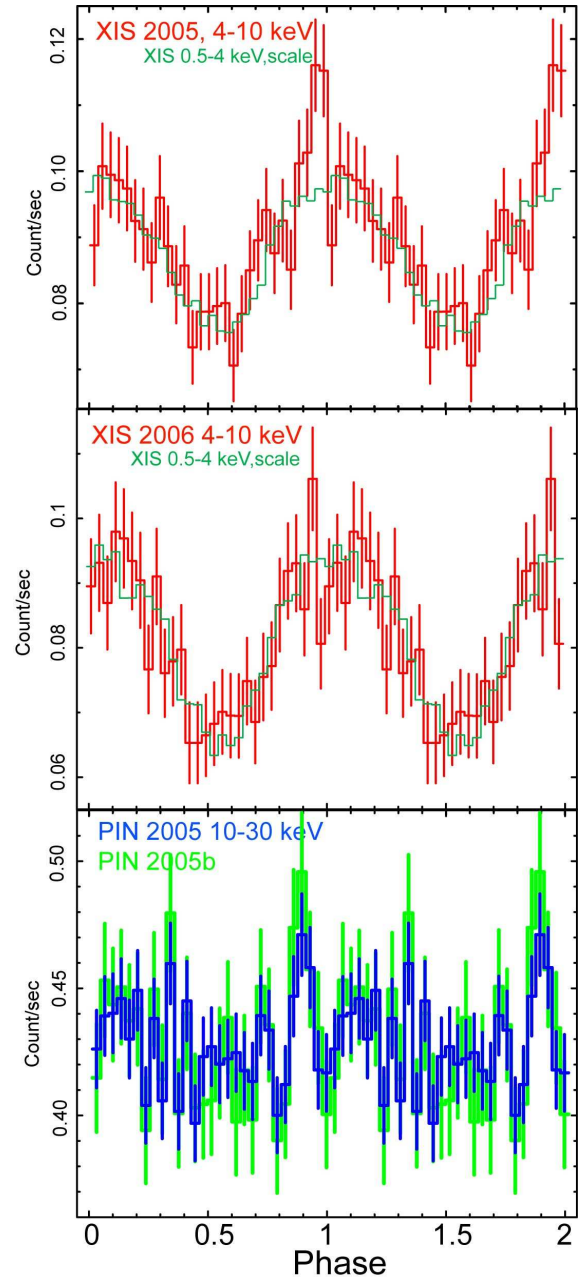

Fig. 4. Soft and hard X-ray profiles of AE Aqr, folded on the HXD-determined period $P_{\rm HXD}$. Phase 0.0 corresponds to BJD 2453673.5000. See the text for the relative XIS vs. HXD timing alignment. (Top and middle) Background-inclusive 0.5–4 keV (green) and $4 - 10$ keV (in red) XIS profiles acquired in 2005 and 2006, respectively. The 0.4–4 keV profile is arbitrarily scaled to approximately agrees with the $4 - 10$ keV profile. (Bottom) The background-inclusive 10–30 keV HXD-PIN data, taken in the entire 2005 observation in blue and the second half of 2005 in green.

bottom, the 2005 PIN signal modulation becomes stronger when we limit the data to the second half (2005b) in agreement with the inference from the periodogram (figure 2); the modulation amplitude of the spike changes from 0.03 $\pm$ 0.01 c s^{-1} to 0.05 $\pm$ 0.01 c s^{-1}. Importantly, a similar spike is also observed at $\phi \sim 0.95$ in the 4−10 keV XIS pro-

file in 2005 (figure 4), superposed on the approximately sinusoidal intensity modulation which dominates the spin-folded profiles in lower energies. As seen in figure 4 (middle), the sharp features in the 4 – 10 keV XIS profile is found also from the 2006 data, but with a reduced amplitude, in agreement with the negative detection of the periodic signal in the 2006 PIN data (section 3.3).

In figure 4, the major sharp spike shows a slight phase difference by $\phi \sim 0.05$ between the XIS (4–10 keV) and PIN data sets. This could be either real or instrumental, because the relative timing between the XIS and HXD is accurate only to within $\sim \pm 0.5$ s even though the absolute timing of the HXD has been verified to an accuracy of $360\ \mu$s (Terada et al. 2008). In order to study at which energy this spike appears, and to examine whether the major spike exhibits any energy-dependent phase shift, we cross-correlated the energy-sorted XIS profiles of the 2005 observation (figure 3 left) against the pulse template from the PIN data (i.e., figure 4 bottom). The results, shown in figure 5, reveals a phase discontinuity at about 4 keV. This means that the XIS profile below 4 keV is dominated by the sinusoidal modulation, and the separate spike starts appearing above 4 keV. Since the cross-correlation peak is thus found consistently at $\phi \sim -0.06$ over the 4 – 10 keV energy band of the XIS, the apparent phase difference (by $\phi \sim 0.05$) seen in figure 4 between the XIS (4–10 keV) and PIN profiles is likely to be instrumental rather than real.

Based on the close similarity between the 4–10 keV XIS folded profile and those from HXD-PIN, we conclude that the periodicity in the PIN signal (at least in 2005b) is in fact due to the WD rotation, and hence AE Aqr emits, at least occasionally, and at least in the 4-30 keV band, a periodic hard X-ray emission component whose folded profile consists of a few sharp pulses.
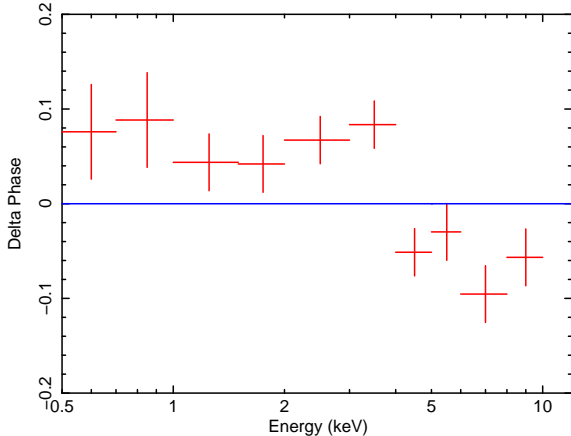

Fig. 5. Energy dependence of the phase of the XIS pulse profiles from the 2005 observation, relative to the 10 – 30 keV PIN profile. The vertical axis shows the phase at which the cross correlation value of each profile to the PIN profile becomes maximum. The folded XIS profiles refer to figure 3 (left), while that of HXD-PIN the 2005 data in figure 4 (bottom).

3.5. Other issues

While we have so far concentrated on the signal modulation at the spin period $P_{\rm sp}$, the signals could also be modulated at beat periods between the rotational and orbital periods, namely at so-called prograde period $P_{\rm pro} = (P_{\rm sp}^{-1} - P_{\rm orb}^{-1})^{-1} = 33.1075$ s, or retrograde period $P_{\rm ret} = (P_{\rm sp}^{-1} + P_{\rm orb}^{-1})^{-1} = 33.0460$ s. If, for instance, the WD is rotating in the same sense as its binary motion, and the X-ray emission region is stationary when observed from a frame of reference co-rotating with the binary, the signals would be modulated at $P_{\rm pro}$ rather than at $P_{\rm sp}$. Indeed, the 2005a PIN periodogram (figure 2 left) exhibits the highest peak at 33.1080 ± 0.0003 s, which is close to $P_{\rm pro}$. All the XIS periodograms (figure 2) also show some enhancements at $\sim P_{\rm pro}$. However, the peak in the 2005a PIN periodogram is slightly (but significantly) offset from the exact $P_{\rm pro}$. Moreover, the 2005b PIN data exhibit no significant modulation at $P_{\rm pro}$, nor at $P_{\rm ret}$. Therefore, we conclude that the hard X-ray periodicity at the beat periods are less convincing, and defer further examination to a future publication.

Since the WD in AE Aqr has a projected orbital semi-major axis of ~ 2 l-s around the binary center of gravity, the X-ray pulse arrival times are expected to vary by this amount depending on the orbital phase. In fact, Mauche (2006) successfully detected this effect, and determined the orbital modulation amplitude as $A = 2.17 \pm 0.48$ l-s; this is $\pm 8\%$ of the pulsation period. While this may be negligible when the pulse profile is sinusoidal, the orbital effects could have significant effects when it has sharp structures, as is in fact the case with the 2005b PIN data. Therefore, we attempted to correct the arrival times, t, of individual X-ray events by subtracting the expected orbital modulation,

$$\Delta t = A \cos \left[2\pi \left(\frac{t - t_0}{P_{\rm orb}} - \xi \right) \right], \qquad (2)$$

where t_0 is the time of the superior conjunction of the WD, and ξ ($0 \le \xi \le 1$) is any possible phase shift.

Employing the nominal orbital parameters by de Jager et al. (1994), namely $\xi = 0.0$, $t_0 = $ BJD 2445172.2784, and $A = 2.04$ s, where A is consistent within errors (2.04 ± 0.13 s) with the value 2.17 ± 0.48 s by Mauche (2006), we applied the correction of equation (2) to the 4–10 keV XIS data. Then, the periodogram peak at $P_{\rm XIS}$ became indeed higher, with χ^2/ν increasing from 7.8 to 9.2 in 2005, and from 6.5 to 8.0 in 2006. When the same correction is applied to the PIN data, the 2005b periodogram peak at $P_{\rm HXD}$ has also increased from 4.2 to 4.3, although no major effects were observed in the other two PIN periodograms. This reinforces our inference that the hard X-ray pulsation in the 2005b data is due to the WD rotation. When we allowed A and ξ to vary, the 4–10 keV XIS data preferred $A = 1.5 \pm 0.5$ and $\xi = -0.1 \pm 0.1$, which are not much different from the nominal ephemeris. Although errors are large, the 2005b PIN data also favor these parameter regions.
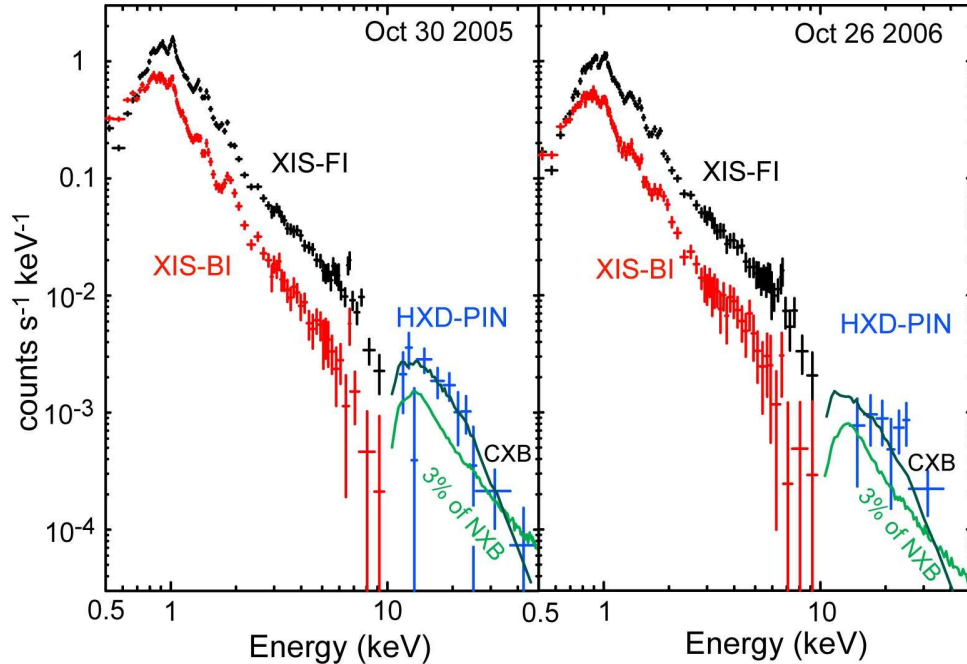
Fig. 6. Background-subtracted spectra of AE Aqr obtained with Suzaku in 2005 and 2006 (left and right, respectively) presented without removing the instrumental responses; error bars are statistical only. The light green curves show the typical uncertainty of the PIN non X-ray background, and the dark green curves indicates the expected cosmic X-ray background (Boldt 1987).

4. Spectral Analyses

To study the origin of the pulsating hard X-ray component revealed in the timing analyses (section 3), we analyzed the pulse phase-averaged spectra taken with the XIS and the HXD. In this analyses, we discarded half the PIN data acquired in 2006, under the reduced voltage of 400V, because the PIN response under this non-standard operation condition is not yet fully calibrated.

The background-subtracted X-ray spectra of AE Aqr obtained in this way are shown in figure 6. In agreement with the inference made in section 3.1, the signal detection with the HXD is significant both in 2005 and 2006, up to ~ 25 keV. This statement remains valid even if we consider the systematic errors in the PIN NXB subtraction, which is estimated to be ~ 3 % in the present case as judged from the reproducibility of the Earth occultation data. However, as shown in figure 6, the PIN detection becomes marginal when we consider the CXB contribution. Therefore, we further subtracted the CXB from the spectra, and summed the result over two observations. As plotted in figure 7a, we obtained positive PIN signals at a level of $\sim 2 \times 10^{-4}$ c s^{-1} kev^{-1} around 20 keV. Thus the source has been detected up to ~ 25 keV. There, the green line in the figure represents the phase-averaged 13 – 30 keV count rate of the spiky signals, $\sim 1.5 \times 10^{-4}$ c s^{-1} keV^{-1}, obtained as a difference between the pulse-peak phase ($\phi = $ -0.1 – 0.1) and the other phase in figure 4 (bottom). The good agreement in figure 7a, between the spectral and timing results from HXD-PIN, indicates that the emission in the PIN range is pulsating nearly 100%.

The phase averaged X-ray spectra of AE Aqr has

been shown with ASCA and XMM-Newton (Choi et al. 1999; Itoh et al. 2006) to be reproduced by an optically thin thermal plasma emission model with a few different temperature components. Thus, to reproduce the Suzaku spectra in the 0.5 – 25 keV band, we adopted a multi-temperature VMEKAL model (Mewe et al. 1995; Liedahl et al. 1995) which are constrained to have common metal abundances but allowed to have separate temperatures. These components were subjected to a common photo-electric absorption with a free neutral column density. The overall model normalization was constrained to be the same between the XIS and PIN. In the fitting, we ignored the systematic errors in the PIN NXB estimation, because the PIN flux was consistent with the pulse flux in the spin profile as already described. As summarized in table 1 (noted as "2005+2006"), the spectra were roughly reproduced by three VMEKAL components, and the derived abundances are consistent with those by XMM-Newton (Itoh et al. 2006). However, the fit was unacceptable with large reduced chi-squared values of 1.79, and was not improved even if we added another VMEKAL component. In addition, the model fell an order of magnitude short of the PIN data.

The large value of reduced chi-squared from the three-temperature VMEKAL fit (table 1) is mainly caused by disagreements between the model and the data around 1 keV, where the Fe-L line complex is present. Thus, we ignored the data below 1.5 keV and fitted the 1.5 – 25 keV data with two VMEKAL components, whose abundances were fixed to the values by Itoh et al. (2006) for simplicity. As shown in figure 7b and listed in table 2, the fit became much improved with reasonable temperatures of $2.90^{+0.20}_{-0.16}$

Table 1. Best fit parameters of the multi temperature VMEKAL Model to the phase averaged spectra.

	XMM-Newton 2001[*]	2005	2006	2005+2006
$N_{\rm H}$ (10^{20}cm^{-2})	$3.59^{+1.47}_{-1.20}$	< 1.28	< 2.04	< 1.92
kT_1 (keV)	$4.60^{+0.60}_{-0.47}$	$3.17^{+0.25}_{-0.15}$	$3.19^{+0.65}_{-0.35}$	$3.04^{+0.14}_{-0.22}$
kT_2 (keV)	$1.21^{+0.13}_{-0.08}$	$0.93^{+0.05}_{-0.08}$	$0.87^{+0.07}_{-0.13}$	0.86 ± 0.06
kT_3 (keV)	0.59 ± 0.02	$0.53^{+0.02}_{-0.03}$	$0.50^{+0.04}_{-0.07}$	$0.50^{+0.04}_{-0.05}$
kT_4 (keV)	$0.14^{+0.05}_{-0.02}$	$-$	$-$	$-$
N (Abundance[†])	$3.51^{+0.92}_{-0.81}$	3.51 fix	3.51 fix	3.51 fix
O (Abundance[†])	$0.74^{+0.17}_{-0.23}$	$0.66^{+0.09}_{-0.10}$	0.57 ± 0.16	$0.64^{+0.09}_{-0.05}$
Ne (Abundance[†])	$0.43^{+0.28}_{-0.25}$	0.66 ± 0.17	$0.49^{+0.26}_{-0.18}$	$0.68^{+0.14}_{-0.16}$
Mg (Abundance[†])	$0.70^{+0.15}_{-0.14}$	$0.76^{+0.10}_{-0.13}$	$0.68^{+0.22}_{-0.18}$	0.77 ± 0.12
Si (Abundance[†])	$0.81^{+0.14}_{-0.12}$	$0.65^{+0.09}_{-0.11}$	$0.43^{+0.13}_{-0.12}$	$0.58^{+0.09}_{-0.10}$
S (Abundance[†])	$0.73^{+0.20}_{-0.18}$	0.89 ± 0.15	0.70 ± 0.19	0.80 ± 0.15
Ar (Abundance[†])	< 0.89	$0.67^{+0.45}_{-0.43}$	$0.31^{+0.66}_{-0.41}$	$0.55^{+0.47}_{-0.46}$
Ca (Abundance[†])	< 1.11	$0.37^{+0.53}_{-0.37}$	0.83 ± 0.80	$0.68^{+0.59}_{-0.60}$
Fe (Abundance[†])	$0.47^{+0.07}_{-0.06}$	$0.40^{+0.04}_{-0.05}$	0.33 ± 0.07	$0.39^{+0.04}_{-0.02}$
Ni (Abundance[†])	$1.27^{+0.57}_{-0.50}$	$1.36^{+0.37}_{-0.39}$	$0.89^{+0.54}_{-0.42}$	$1.14^{+0.31}_{-0.34}$
Flux[‡](10^{-12} erg s^{-1} cm^{-2})	11.6	$6.83^{+0.33}_{-0.26}$	$6.22^{+0.38}_{-0.24}$	$6.65^{+0.20}_{-0.29}$
χ^2_ν(dof)	1.22(992)	1.94(152)	1.45(152)	1.79(152)

[*] From Itoh et al. (2006).
[†] Solar abundances by Anders and Grevesse (1989).
[‡] In the 0.5 – 10 keV band.

keV and $0.53^{+0.14}_{-0.13}$ keV. However, the model still disagrees with the PIN data points.

To reproduce the PIN flux, we added an additional power-law component to the two VMEKAL model, and obtained an acceptable result as shown in figure 7c and table 2. The F-statistic of this improvement is 15.5, which means that the probability of this improvement being caused by chance is 2.0×10^{-6}. Thus, adding another component is justified. The power-law modeling is, however, not unique, and another VMEKAL model instead of the power-law model also provides a significantly improved fit at a temperature of 54^{+26}_{-47} keV (table 2), with the F-test value of 11.1 or the chance probability of 3.5×10^{-6}. The derived temperature is essentially considered a lower limit, i.e., > 7 keV. Since a thermal component of such a temperature is not rare among accreting WDs, we cannot distinguish, from the spectral analysis alone, whether the additional hard X-ray component detected with the HXD is thermal or non-thermal.

5. Discussion

5.1. Summary of the Observation

Using Suzaku, we observed AE Aqr in 2005 and 2006. In the first observation, the HXD detected periodic signals synchronized with the rotation of the WD (section 3.3) whose profile has a sharp peak (section 3.4) with a duration of $\sim$0.1 in phase. The same sharp feature was also found in the spin-folded XIS light curves in energies above 4 keV. The phase-averaged spectra from the XIS above 1.5 keV can be explained with the two optically thin thermal plasma models with temperatures of $2.90^{+0.20}_{-0.16}$ keV and $0.53^{+0.14}_{-0.13}$ keV (section 4). The PIN spectrum up to

25 keV, however, shows an excess emission over the model. This excess can be fitted by a power-law model with a photon index of 1.1 ± 0.6, or another thermal model with the temperature of 54^{+26}_{-47} keV. In the 13–30 keV range, the spectrally measured excess, $3.2^{+9.7}_{-2.5}$ c s^{-1}, is consistent within large errors with that contained in the sharp peaks in the spin-folded hard X-ray light curves.

The 4–30 keV flux of the additional hard component from the spectral analyses is obtained as $L_{\rm HX} \sim 1.7^{+4.9}_{-0.1} \times 10^{-12}$ erg cm^{-2} s^{-1}, which gives a luminosity of $5.3^{+15.3}_{-0.3} \times 10^{29}$ erg s^{-1} at the distance of 102 pc (Friedjung 1997). This corresponds to $\sim 0.01\%$ of the spin-down luminosity of 6×10^{33} erg s^{-1} (de Jager 1994; de Jager et al. 1994). Note, however, that the hard X-ray pulsation has a duty ratio of only $\sim$0.1. If the hard X-ray emission is highly anisotropic without a constant bias, and if the emission is beamed away from us in the other pulse phases, the true hard X-ray luminosity would be higher, amounting up to 5×10^{30} erg s^{-1} which is 0.1% of the spin-down luminosity. In any case, the ratio of the hard X-ray emission to the spin-down luminosity of AE Aqr comes in the range of 0.01–0.1%, which is the same as those measured in the 2–10 keV range from NS pulsars (Becker and Truemper 1997; Possenti et al. 2002).

5.2. The Nature of the Hard X-ray Component

The observed hard X-ray emission pulsates at the WD rotation period, but not at the prograde or retrograde beat periods. In order to reinforce this result, we further folded the 4–10 keV XIS data at the prograde and retrograde beat periods, but the results were consistent with the absence of any periodic modulation, either in the 2005 or 2006 data sets. This implies that the hard X-ray emis-

Table 2. Best Fit Parameters of the multi temperature VMEKAL[†] with/without Power Law model to the phase averaged spectra in the 1.5 – 25 keV band.

Model[*]	$N_{\rm H}$[†]	kT_1[‡]	Flux[§]	kT_2[‡]	Flux[§]	Photon Index or kT_3[‡]	Flux[§]	χ^2_ν (dof)
i	< 0.165	$2.90^{+0.20}_{-0.16}$	$3.77^{+0.30}_{-0.18}$	$0.53^{+0.14}_{-0.13}$	$3.18^{+4.61}_{-0.97}$	–	–	1.27 (84)
ii	$0.66^{+0.36}_{-0.38}$	$2.04^{+0.09}_{-0.21}$	$1.96^{+0.32}_{-0.37}$	$0.27^{+0.05}_{-0.05}$	$0.74^{+1.64}_{-0.56}$	$1.12^{+0.63}_{-0.62}$	$0.59^{+1.80}_{-0.05}$	0.95 (82)
iii	$0.67^{+0.17}_{-0.20}$	$2.01^{+0.17}_{-0.23}$	$2.13^{+0.03}_{-0.64}$	$0.26^{+0.07}_{-0.04}$	$3.82^{+6.86}_{-2.83}$	$54.4^{+25.7}_{-47.2}$	$0.66^{+11.9}_{-0.20}$	0.95 (82)

[*] Abundances are fixed to the XMM-Newton values (Itoh et al. 2006). Model (i) is double VMEKAL, (ii) is double VMEKAL with power law, and (iii) is triple VMEKAL mode.
[†] Column density in 10^{20} cm^{-2}.
[‡] Temperature in keV.
[§] Flux in 10^{-12} erg s^{-1} cm^{-2} in 0.5 – 10 keV.

sion region is fixed in the frame which is co-rotating with the WD, while excludes a possibility that the emission region is fixed to the binary frame.

Although approximately in phase with the soft X-ray spin modulation, the hard X-ray pulses exhibit a spiky profile with a duty ratio of only ~ 0.1 in phase, unlike the sinusoidal profile in the XIS band below 4 keV. Furthermore, the spin phase of the major spike exhibits an energy dependence with a discontinuity at ~ 4 keV (figure 5). The soft and hard X-ray components are therefore likely to originate from distinct emission sites. If interpreted as hot thermal emission, the hard component, with its very high temperature, should be emitted from the bottom of the gravitational potential, i.e., the WD surface, while the softer component from some outer regions (Itoh et al. 2006). However, it would be highly difficult to produce the observed sharp pulse profiles from the WD surface (e.g., magnetic poles) via any thermal process. Indeed, such X-ray pulsations, appearing only in the hard X-ray band with very sharp profiles, have never been observed from other accreting magnetic WDs (Terada et al. 2004), in which the thermal emission mechanism is considered to dominate. We thus consider that the hard component is more naturally interpreted as non-thermal emission, as evidenced by its successful power-law modeling. If so, a population of non-thermal particles must be accelerated in the AE Aqr system, at least occasionally, producing the hard X-ray pulses detected with Suzaku. In the following two subsections, we discuss possible particle acceleration mechanisms, and hard X-ray emission mechanisms from the accelerated electrons.

5.3. Possible Acceleration Mechanism

As mentioned in section 1, the fast rotating WD in the AE Aqr system is expected to produce an induced electric potential reaching $V \simeq 10^{14-15}$ V. Therefore, it is most natural to assume that the non-thermal particles are acceleration by this electric potential.

Although the suggested acceleration mechanism is very similar to that in rotation-powered pulsars, the present WD system differs from pulsars in an important physical condition. While a rotation-powered pulsar is expected to reside in a low-density environment, AE Aqr is an accreting binary system. In particular, the radius of the light cylinder, $l_{\rm lc} \sim P_{\rm sp}/2\pi \sim 5$ l-s, is comparable to the binary size of ~ 6 l-s. In fact, Itoh et al. (2006), analyz-

ing the XMM-Newton RGS data of AE Aqr, concluded that a plasma with the electron density $n_{\rm e} \sim 10^{11}$ cm^{-3} is spread over a scale of $(2-3) \times 10^{10}$ cm in this binary system. Since this plasma density exceeds the Godreich-Julian density (Goldreich and Julian 1969) which is calculated as $\sim 5 \times 10^4$ cm^{-3} in the present case (Ikhsanov and Biermann 2006), the induced potential would be short-circuited, and hence an efficient acceleration would not take place. However, both theoretical (Wynn et al. 1997) and observational works suggest that the propeller effect produces a low-density cavity around the WD, by inhibiting the accretion plasma from getting closer to the WD than $\sim 10^{10}$ cm (Wynn et al. 1997). The electric acceleration may be possible in such regions.

Even if the plasma density is sufficiently low, an efficient electric-field acceleration also requires evacuation of neutral matter from the acceleration region; otherwise, the electrons would suffer too heavy ionization losses to be accelerated efficiently. The mean-free-path of an electron with energy $E_{\rm e}$, due to ionization loss, is given by

$$\lambda_{\rm e} \sim \frac{1}{n_{\rm p}} \frac{1}{\ln\Lambda} \left(\frac{\pi e^2}{8\epsilon_0 E_{\rm e}} \right)^{-2}$$
$$\sim 10^7 \left(\frac{n_{\rm p}}{10^{10}{\rm cm}^{-3}} \right)^{-1} \left(\frac{E_{\rm e}}{1{\rm keV}} \right)^2 {\rm cm}, \qquad (3)$$

where $n_{\rm p}$ is the density of protons, $\ln\Lambda$ is a Coulomb logarithm (typically $\sim 10 - 20$), e is the elementary charge, and ϵ_0 is the vacuum dielectric constant (see e.g., Rybichi & Lightman 1979). If an initial electron energy is $E_{\rm e} \sim 1$ keV assuming a thermal plasma in the system, the energy gain of the electron accelerated along the length of $\lambda_{\rm e}$ can be roughly estimated to be $E_{\rm acc} \sim \frac{V}{l_{\rm lc}} \cdot \lambda_{\rm e} \sim 10^{10} \left(\frac{n_{\rm p}}{10^{10}{\rm cm}^{-3}} \right)^{-1}$ eV, with $V \sim 10^{14}$ V and $l_{\rm lc} \sim 10^{11}$ cm. Thus, the energy gain $E_{\rm acc}$ exceeds the initial energy $E_{\rm e}$ when the surrounding density is $n_{\rm p} < 10^{17}$ cm^{-3}. Therefore, in the AE Aqr system with $\sim 10^{11}$ cm^{-3} (Itoh et al. 2006), the ionization loss does not affect the electron acceleration.

5.4. The Hard X-ray Emission Mechanism

In general, there are the following four elementary processes that can produce hard X-ray emission from accelerated electrons: non-thermal bremsstrahlung, inverse Compton scattering, synchrotron emission, and curvature
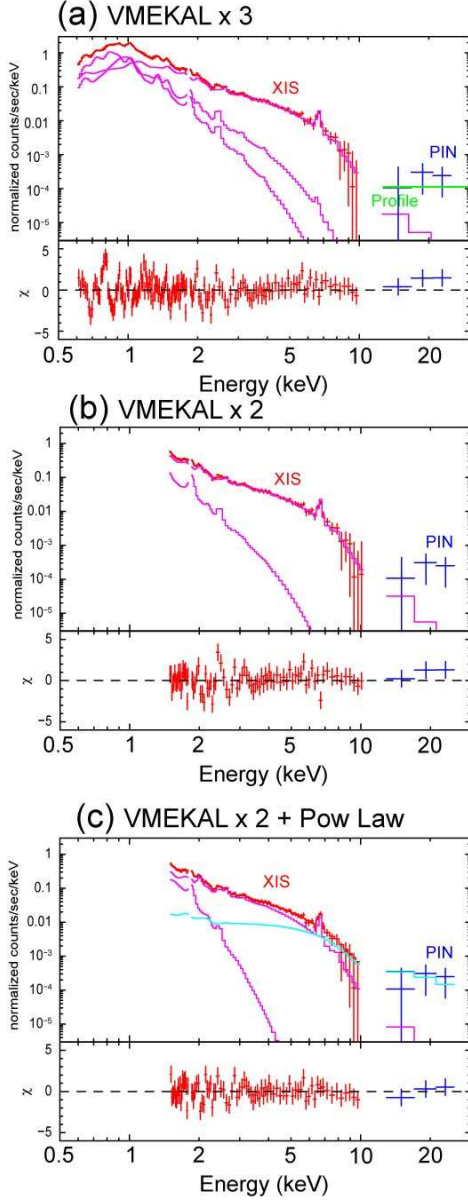
Fig. 7. Model fits to the phase-average Suzaku spectra, summed over the two observations (2005 and 2006). Red and blue crosses show the XIS and PIN data, respectively, from which the NXB and CXB have been subtracted. (a) A fit with a three-temperature VMEKAL model in the 0.5 – 25 keV band, with the parameters listed in table 1 (labeled as 2005+2006). The horizontal green line indicates the 13–30 keV PIN X-ray count rate obtained from the folded pulse profile (figure 4 bottom), as a difference between $\phi = -0.1 - 0.1$ and $\phi = 0.1 - 0.9$. (b) A fit with a two-temperature VMEKAL model, in the 1.5 – 25 keV band. The best-fit parameters are listed in table 2. (c) The same as panel (b), but a power-law with photon index of 1.12 (cyan) is added.

radiation. Considering the observational results, we examine these processes.

If the hard X-rays are due to non-thermal bremsstrahlung in thick materials, electrons have to be accelerated only to an energy of ~ 100 keV to emit X-rays with an energy of several tens of keV. The emanating hard X-ray spectrum is expected to have a photon index of ~ 1, when the target is thick and hence the electrons have a flattened energy distribution due to Coulomb losses (Uchiyama et al. 2002). This is in good agreement with the observed photon index, $1.12^{+0.63}_{-0.62}$. Candidates of the dense matter, co-rotating with the WD, includes the surface of the WD and the accretion stream toward the magnetic poles. However, to produce the sharp hard X-ray pulses, the electrons must be in the form of collimated beams (e.g., along the magnetic field lines), and furthermore, must be moderately relativistic (≥ 200 keV) so that the bremsstrahlung emissivity is sufficiently anisotropic (Koch and Motz 1959) to produce the spike in the hard X-ray light curve. It is not obvious whether these conditions can be fulfilled. Furthermore, a still larger difficulty is in energetics: in the 10 – 100 keV range, an electron loses $\sim 10^4$ times larger energies in ionization (or Coulomb) loss than in radiation. Then, the particle acceleration requires an energy input which is more than an order of magnitude higher than the spin-down luminosity. We therefore conclude that the bremsstrahlung interpretation is difficult.

In the inverse-Compton scenario, the seed photons can be either the UV photons from the WD or the optical photons from the companion star whose spectral type is K3–K5 (Welsh et al. 1995). Then, the electrons are required to have a Lorentz factor of $\gamma \sim 10^2$, or an energy of ~ 100 MeV. The estimated 4–30 keV luminosity (after accounting for the duty ratio; section 5.1) translates to a hard-photon number flux of 2.6×10^{37} s^{-1}. This is a reasonably small fraction ($\sim 10^{-7}$) of the optical photon number flux to be expected from a K4 star ($\simeq 5 \times 10^{44}$ s^{-1} near the WD surface). However, the inverse-Compton process is rather inefficient; an electron with a Lorentz factor $\gamma \simeq 10^2$ is expected to lose half its energy in $T_{1/2} \simeq \frac{1}{\gamma} \frac{m_e c^2}{\sigma_T c u_s} \sim 4 \times 10^6$ s, where m_e is the electron mass, σ_T is the Thomson cross section, and $u_s \simeq 0.1$ erg cm^{-3} is the visible photon density at the position of the WD. Therefore, the electron is expected to leave the system after depositing only $\sim 10^{-6}$ of its energy. The energy input needed to sustain the particle acceleration would be then $\sim 10^6 L_{HX}$, making the inverse Compton scenario highly unlikely.

As the third possibility, we consider synchrotron radiation by relativistic electrons. For a magnetic field strength of $B = B_5 \times 10^5$ G, an electron is required to have a Lorentz factor $\gamma \sim 10^4 B_5^{-1}$ to emit ~ 30 keV photons. This value of γ is lower than the maximum possible energy expected from the induced voltage (section 1) by ~ 4 orders of magnitude. Furthermore, the synchrotron emission is highly efficient, with a very short lifetime of $\sim 8 \times 10^{-6} B_5^{-2} (\frac{\gamma}{10^4})^{-1}$ s (e.g, Reynolds 1998; Vink & Laming 2003). Considering further that the synchrotron emission is highly anisotropic, we presume that this scenario is quite likely, if the electrons are accelerated along the field lines, and then at some stage, acquire cross-field velocity and start emitting synchrotron photons. The observed photon index $\Gamma \sim 1.1$ predicts a very flat electron spectrum with a spectral index of ~ 1.2. This does

not matter, however, if direct electron field acceleration works. In fact, rotation-powered NS pulsars generally exhibit rather flat spectra in X-rays, $\Gamma \sim 1.4$ (Gotthelf 2003).

Finally, we consider the possibility of the curvature radiation process. According to Usov (1988), the energy of the hard X-ray emission via curvature radiation can be written as

$$E \sim \frac{3}{2}\frac{\hbar c\gamma^3}{R_{\rm crv}} \sim 50 \left(\frac{\gamma}{10^6}\right)^3 \left(\frac{R_{\rm crv}}{R_{\rm WD}}\right)^{-1} {\rm keV}, \qquad (4)$$

where $\hbar$ is the Plank constant, $R_{\rm crv}$ is the curvature radius of magnetosphere field lines, and $R_{\rm WD}$ is the WD radius of AE Aqr. On the right-hand side of equation 4, $R_{\rm crv}$ is normalized for convenience to $R_{\rm WD}$. It is not easy to predict where the photon energy E is maximized, because a smaller curvature radius can be realized closer to the WD, whereas the maximum γ is probably achieved at a larger radius. Generally, as we move away from the WD surface, $R_{\rm crv}$ decreases gradually, while γ of the electrons being accelerated will increase rapidly. According to Ikhsanov and Biermann (2006), the curvature-radiation photons will reach the maximum of $E \sim 100$ keV at $R_{\rm crv} \sim l_{\rm lc}$, together with $\gamma \sim 6 \times 10^6$, which is feasible in the AE Aqr system. However, the efficiency of this process is so low that the luminosity is estimated to be $\sim 3 \times 10^{27}$ erg s$^{-1} \sim 10^{-2} L_{\rm HX}$. Therefore, it is difficult to explain the observation in terms of the curvature radiation.

We conclude that the hard X-ray pulse is probably caused by relativistic electrons accelerated by the fast rotation of the magnetized WD. The most promising emission mechanism is the synchrotron emission in the strong magnetic fields of the WD.

Acknowledgements

References

Abada-Simon, M., Latchkey, A., Bastian, T. S., Bookbinder, J. A., & Dulk, G. A. 1993, ApJ, 406, 692

Anders, E. & Grevesse, N. 1989, Geochim. Cosmochim. Acta, 53, 197

Bastian, T. S., Dulk, G. A., & Chanmugam, G. 1988, ApJ, 330, 518

Beasley, A. J., Bastian, T. S., Ball, L., & Wu, K. 1994, AJ, 108, 2207

Becker, W. & Truemper, J. 1997, A&A, 326, 682

Bhat, C. L., Kaul, R. K., Rawat, H. S., Senecha, V. K., Rannot, R. C., Sapru, M. L., Tickoo, A. K., & Razdan, H. 1991, ApJ, 369, 475

Boldt, E. 1987, in IAU Symp. 124 Observational Cosmology, ed. Hewitt, A., Burbidge, G., & Fang, L. Z., 611

Bond, H. E., White, R. L., Becker, R. H., & O'Brien, M. S. 2002, PASP, 114, 1359

Casares, J., Mouchet, M., Martinez-Pais, I. G., & Harlaftis, E. T. 1996, MNRAS, 282, 182

Chanmugam, G. & Brecher, K. 1985, Nature, 313, 767

Chanmugam, G. & Dulk, G. A. 1982, ApJL, 255, L107

Cheng, K. S. & Ruderman, M. 1991, ApJ, 373, 187

Choi, C.-S., Dotani, T., & Agrawal, P. C. 1999, ApJ, 525, 399

de Jager, O. C. 1994, ApJS, 90, 775

de Jager, O. C., Meintjes, P. J., O'Donoghue, D., & Robinson, E. L. 1994, MNRAS, 267, 577

Dulk, G. A., Bastian, T. S., & Chanmugam, G. 1983, ApJ, 273, 249

Eracleous, M. & Horne, K. 1996, ApJ, 471, 427

Ezuka, H. & Ishida, M. 1999, ApJS, 120, 277

Friedjung, M. 1997, New Astronomy, 2, 319

Goldreich, P. & Julian, W. H. 1969, ApJ, 157, 869

Gotthelf, E. V. 2003, ApJ, 591, 361

Ikhsanov, N. R. & Biermann, P. L. 2006, A&A, 445, 305

Itoh, K., Okada, S., Ishida, M., & Kunieda, H. 2006, ApJ, 639, 397

Koyama, K. et al. 2007, PASJ, 59, S23

Kokubun, M. et al. 2007, PASJ, 59, S53

Koch, H., W, & Motz, J., W., 1959, Reviews of Modern Physics, 31, 920

Larsson, S. 1996, A&AS, 117, 197

Liedahl, D. A., Osterheld, A. L., & Goldstein, W. H. 1995, ApJL, 438, L115

Mason, P. A. & Gray, C. L. 2007, ApJ, 660, 662

Mauche, C. W. 2006, MNRAS, 369, 1983

Meintjes, P. J., de Jager, O. C., Raubenheimer, B. C., Nel, H. I., North, A. R., Buckley, D. A. H., & Koen, C. 1994, ApJ, 434, 292

Meintjes, P. J., Raubenheimer, B. C., de Jager, O. C., Brink, C., Nel, H. I., North, A. R., van Urk, G., & Visser, B. 1992, ApJ, 401, 325

Meintjes, P. J. & Venter, L. A. 2003, MNRAS, 341, 891

Mewe, R., Kaastra, J. S., & Liedahl, D. A. 1995, Legacy, 6, 16

Mitsuda, K et al. 2007, PASJ, 59, S1

Nelson, R. F. & Spencer, R. E. 1988, MNRAS, 234, 1105

Patterson, J. 1979, ApJ, 234, 978

Pavelin, P. E., Spencer, R. E., & Davis, R. J. 1994, MNRAS, 269, 779

Possenti, A., Cerutti, R., Colpi, M., & Mereghetti, S. 2002, A&A, 387, 993

Reynolds, S. P. 1998, ApJ, 493, 375

Serlemitsos, P. J. et al. 2007, PASJ59, S9

Takahashi, T., et al. 2007, PASJ, 59, S35

Terada, Y., et al. 2004, PASJ, 56, 533

Terada, Y., et al. 2008, PASJ, 60, in press (#3184)

Rybichi G. B. & Lightman A. P. 1979, Radiative Process in Astrophysics, (Wiley Interscience Publication, New York), ch. 5

Usov, V. V. 1988, Sov. Astron. Lett. 14, 258

Uchiyama, Y., Takahashi, T. Aharonian, F. A. & Mattox, J. R. 2002, ApJ, 571, 866

Vink, Y., & Laming, J. M., 2003, ApJ, 584, 758

Watanabe, S., et al. 2007, Suzaku memo 2007-01-24, 1, see http://www.astro.isas.jaxa.jp/suzaku/doc/suzakumemo/suzakumemo-2007-01.pdf

Welsh, W. F., Horne, K. & Gomer, R. 1993, ApJL, 410, L39

Welsh, W. F., Horne, K., & Gomer, R. 1995, MNRAS, 275, 649

Wynn, G. A., King, A. R., & Horne, K. 1997, MNRAS, 286, 436